

JGR Space Physics

RESEARCH ARTICLE

10.1029/2021JA029438

Key Points:

- Microinstabilities play a role in limiting proton temperature anisotropy (both $\frac{T_{\perp p}}{T_{\parallel p}} > 1$ and $\frac{T_{\perp p}}{T_{\parallel p}} < 1$) upstream of Mars
- Probability density functions of magnetic field fluctuations exhibit intermittent structures present in upstream plasma at Mars
- Spectral indices obtained from power spectral densities of magnetic field fluctuations demonstrated a power law decay for inertial ranges

Supporting Information:

Supporting Information may be found in the online version of this article.

Correspondence to:

C. L. Lentz,
christy.lentz@lasp.colorado.edu

Citation:

Lentz, C. L., Chasapis, A., Qudsi, R. A., Halekas, J., Maruca, B. A., Andersson, L., & Baker, D. N. (2021). On the solar wind proton temperature anisotropy at Mars' orbital location. *Journal of Geophysical Research: Space Physics*, 126, e2021JA029438. <https://doi.org/10.1029/2021JA029438>

Received 12 APR 2021

Accepted 2 SEP 2021

On the Solar Wind Proton Temperature Anisotropy at Mars' Orbital Location

C. L. Lentz¹ , A. Chasapis¹, R. A. Qudsi² , J. Halekas³ , B. A. Maruca², L. Andersson¹ , and D. N. Baker¹ 

¹Laboratory for Atmospheric and Space Physics, University of Colorado, Boulder, CO, USA, ²Department of Physics and Astronomy, University of Delaware, Newark, DE, USA, ³Department of Physics and Astronomy, University of Iowa, Iowa City, IA, USA

Abstract The Mars Atmosphere and Volatile Evolution (MAVEN) spacecraft can act as an intermittent upstream solar wind monitor at ~1.5 AU. To inspect the evolution of solar wind turbulence in the Martian exosphere, we have gathered proton (i.e., ionized hydrogen) temperature measurements taken by the Solar Wind Ion Analyzer (SWIA) onboard the MAVEN spacecraft. Here we investigate instabilities driven by the proton temperature anisotropy at Mars during southern hemisphere fall, winter, spring, and summer seasons. We look at the relationship between the temperature anisotropy, $R_p = T_{\perp p}/T_{\parallel p}$ (i.e., the ratio of the perpendicular proton temperature component to the parallel proton temperature component), and the parallel plasma beta, $\beta_{\parallel p}$, to determine any constraints imposed by kinetic instabilities. Furthermore, we report on the properties of turbulence near Mars' orbital location during upstream solar wind intervals from January 2015 to December 2016 (~1 Martian year). We find that the probability distributions of ($\beta_{\parallel p}$, R_p)-values become limited when R_p deviates greatly from unity. We also find evidence of intermittency implying nonlinear, non-homogeneous energy transfer. Additionally, spectral indices obtained from basic fittings of power spectral densities of magnetic field fluctuations demonstrate a power law decay for inertial ranges (10^{-4} Hz to 0.1 Hz).

Plain Language Summary Radially emanating from the Sun, solar wind consists of highly ionized and strongly magnetized plasma. During its expansion, the solar wind develops into a turbulent flow. With increasing distance from the Sun, one would expect the temperature of protons in the solar wind to decrease at a certain rate. Instead, we see that protons are hotter than expected, and therefore some heating mechanism must be at work. One such mechanism can be turbulence. The energy of turbulent motions is converted into heat at small, proton gyroradius-sized scales. This can cause the proton temperature components to become unequal when measured along axes in different directions, known as the proton temperature anisotropy. While there have been multiple spacecraft to characterize turbulence and proton temperature anisotropies at 1 AU, there exist limited opportunities to obtain these same measurements beyond this orbital location. To study the basic properties of turbulence and proton temperature anisotropies at Mars' orbital location, we used the Mars Atmosphere and Volatile Evolution spacecraft.

1. Introduction

1.1. Turbulence in the Solar Wind

Solar wind is a supersonic and super Alfvénic plasma flow originating from the Sun. It is a continuously expanding plasma that is highly ionized and threaded with large scale magnetic fields (Bruno & Carbone, 2016). The thermodynamic adiabatic expansion law applied to proton temperatures in the solar wind would suggest that temperature declines with heliocentric distance as $T(r) \sim r^{-\frac{4}{3}}$. Instead, solar wind evolves in a highly non-trivial way as it expands from the Sun (e.g., Matteini et al., 2007). There exist numerous observations to imply that some heating mechanism must be at work within the solar wind to supply the energy required to slow down the decay (Pine et al., 2020).

One potential explanation for this heating is turbulence. As the highly ionized and magnetized solar wind develops into a turbulent flow at large scales, it can act as a reservoir of energy. As eddies in the turbulent

plasma interact, they break up into smaller eddies, undergoing what is known as an energy cascade. In this energy cascade, there is a net transfer of energy from large scales where turbulence first develops, to small scales where dissipative mechanisms convert turbulent energy to heat (Bruno & Carbone, 2016; Howes, 2008; Klein & Howes, 2015; Verscharen et al., 2019).

The turbulent effects of the plasma can be described in a magnetohydrodynamic (MHD) framework (Matthaeus & Goldstein, 1982). The flow can also be described by hydrodynamic turbulence at low frequencies and long wavelengths (Kolmogorov, 1941a, 1941b). Plasma instabilities and associated wave particle interactions play a role in all observations at 1 AU. However, studies of solar wind turbulence beyond 1 AU have generally been limited by instrument capabilities. The exceptions being the Ulysses and Voyager missions (see e.g., Horbury et al. (2008), Pine et al. (2020) and references therein for examples of such studies).

To inspect the evolution of solar wind turbulence and proton temperature anisotropies in and upstream of the Martian atmosphere, we have gathered magnetic field data (MAG; Connerney et al., 2015) and proton temperature measurements taken by the Solar Wind Ion Analyzer (SWIA; Halekas et al., 2015) both onboard the MAVEN spacecraft. Here we examine Probability Distribution Functions (PDFs) and Power Spectral Densities (PSDs) of magnetic field fluctuations to report on solar wind turbulence near Mars' orbital location. Furthermore, we investigate instabilities driven by the proton temperature anisotropy at Mars. These results provide novel insights into the physics of solar wind around Mars and contribute to the understanding of the role turbulence and plasma instabilities play in the evolution of the solar wind.

1.2. The Martian Plasma Environment

Mars acts as an obstacle to the supersonic and magnetized plasma emanating from the Sun. A shock wave is formed in front of the planet known as the bow shock. It serves to slow down the flowing solar wind from supersonic to subsonic speeds (Luhmann, 1992; Mazelle et al., 2004). Plasma thermalization then occurs in the sheath, at and downstream of the shock (Luhmann, 1992).

One fascinating feature of Mars is an exosphere that extends beyond the bow shock due to the weaker gravity of the planet (Mazelle et al., 2004). Above the exobase (altitude ~ 200 km; Bhattacharyya et al., 2017) an extended exosphere is formed in part due to the ballistic motion of hydrogen atoms (Anderson, 1974; Anderson & Hord, 1971; Chaffin et al., 2015; Chaufray et al., 2008). There is known to be a high degree of variability of the hydrogen density of the exosphere, with peak hydrogen densities occurring at Solar Longitude (L_s) values $\sim 263^\circ - 288^\circ$, roughly centered on Mars southern summer solstice ($L_s = 270^\circ$; Halekas, 2017). Where L_s is the Mars-Sun angle measured from the Northern Hemisphere Spring equinox ($L_s = 0^\circ$). This causes the solar wind/Mars interaction and therefore upstream dynamics at Mars to be very complex.

Further differences between plasma properties at Earth and Mars arise from Mars' greater heliocentric distance and its smaller size. The lower solar wind density and interplanetary magnetic field (IMF) strength make for a different Mach number. Due to the smaller planet size and diminished IMF strength, the gyroradius of solar wind protons is comparable to the size of the shock, making kinetic effects important (Mazelle et al., 2004).

Few studies have investigated turbulence at Mars. Ruhunusiri et al. (2017) was the first known study to characterize turbulence in the Martian plasma environment. They determined that turbulence characteristics at Mars vary seasonally. Additionally, they found that a fully developed energy cascade is absent in the magnetosheath of Mars, but present in the magnetic pileup boundary (also known as the induced magnetosphere boundary; see Espley, 2018 for a debate on the nomenclature). A study conducted by Andrés et al. (2020) estimated the incompressible energy cascade rate at MHD scales in the plasma upstream of the bow shock for events with and without proton cyclotron wave activity. To date, there have been no known studies that examine the proton temperature anisotropy at Mars. The aim of this article is to provide an evaluation of temperature anisotropy instabilities.

2. Methodology

2.1. MAVEN Data

In order to analyze plasma instabilities and associated wave-particle interactions at Mars' orbital location we used SWIA to obtain 3D distributions of proton temperature moments. SWIA is an electrostatic analyzer designed to measure solar wind and magnetospheric ions in the Martian planetary environment. Among other quantities, temperature is calculated on board from SWIA coarse data when MAVEN is in the sheath, or fine data when MAVEN is in its solar wind mode. A few caveats of note are that moments are computed assuming the entire distribution is within the field of view and energy range of SWIA. Also, the assumption that all ions are protons is made which can be problematic when looking into the data quantitatively. The upstream solar wind consists of ~94%–97% ions as protons and ~3%–6% alpha particles (Liu et al., 2021). Any alpha particles present in the distribution, with which SWIA is using to compute the temperature moments, can lead to artificially large values. This effect is most prominent in the flow-aligned component of the temperature moment. Another potential complication arises when attempting to completely resolve temperatures when cold plasma beams are being sampled. This is due to the ~15% energy resolution of SWIA. However, proton temperatures can be more accurately calculated by taking SWIA level 2 3D fine data and separately computing proton and alpha temperature moments using a routine discussed in Halekas et al. (2017).

Alpha particles are typically separated along the magnetic field from the protons. By locating proton and alpha peaks in the 3D distributions, the energy between them can be bisected. Everything on the alpha side of the break is then disregarded, and the proton moments are then calculated. When thermal velocity is small compared to bulk velocity, alpha particles show up at twice the energy per charge than protons, and therefore can be separated. This is challenging to do so with really hot distributions, as SWIA does not have mass resolution capabilities. This causes difficulty in discerning proton and alpha peaks because they overlap in hot distributions. However, for the purpose of this study, only time intervals of undisturbed solar wind were used based on the criteria outlined in Section 3.1 of Halekas et al. (2017). The routine, therefore, successfully generates x, y, and z components of proton temperatures in magnetic field aligned coordinates. The z component is $T_{\parallel p}$, or the parallel proton temperature component. The average of the x and y components is taken to be $T_{\perp p}$, or the perpendicular temperature component.

MAG DC measurements were used to calculate the parallel plasma beta component ($\beta_{\parallel p}$) and to facilitate solar wind interval identification. Two tri-axial fluxgate magnetometer sensors measure the vector magnetic field throughout the Martian plasma environment over a wide dynamic range with a resolution up to 0.008 nT at an accuracy of ~0.05%. The better of the two magnetometers are used to sample the ambient magnetic field at a rate of 32 vector samples per second and create the standard data product.

Although it is debatable if MAVEN's orbit ever encounters truly pristine upstream solar wind at Mars due to the exosphere, there is still plenty of information that can be gleaned about turbulence and temperature anisotropies. Upstream solar wind intervals were identified for the 1st through the 10th of each month from January 2015 to December 2016. The number of intervals each month were limited by the availability of the proton temperature moments. Upstream solar wind periods at Mars were recognized in the magnetic field by diminished fluctuations in the magnetic field components, and low vector magnitude ($|\vec{B}_{sw}| \leq 10 \text{ nT}$) compared to other plasma regions and boundaries. The typical density rose no higher than 10 protons per cubic centimeter ($\rho \leq 10 \text{ cm}^{-3}$). There was also a steady negative x component of the velocity ($\vec{V}_x < 0$).

From these intervals turbulent statistics and temperature anisotropies were then calculated. To access the start and stop times along with maxima, minima, medians, and averages of every parameter discussed in this study, please refer Table S1. The solar wind intervals were then classified into southern hemisphere Martian seasons using the L_s values. $0^\circ \leq L_s \leq 89^\circ$ represents the Martian fall season, winter values span $90^\circ \leq L_s \leq 179^\circ$, $180^\circ \leq L_s \leq 269^\circ$ corresponds to spring, and $270^\circ \leq L_s \leq 359^\circ$ corresponds to summer. For this study, 2015-07-01 to 2016-01-03 corresponded to Autumn. Winter times were 2016-01-04 to 2016-07-04. Spring mapped to the time periods 2015-01 and from 2016-07-04 to 2016-11. Summer months were from 2015-02 to 2015-06, and 2016-12.

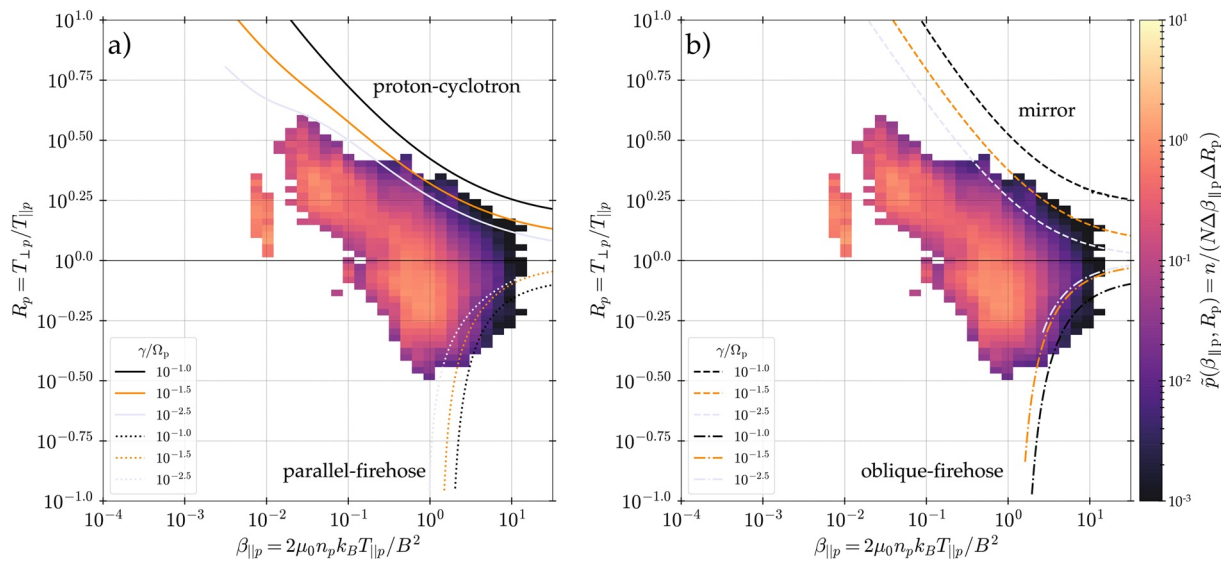


Figure 1. Probability distributions of $(\beta_{\parallel p}, R_p)$ -values for statistically significant bins from January 2015 to December 2016. Plot (a) depicts probability distributions with contours of constant growth rate (normalized by the proton cyclotron frequency $[\Omega_p]$) for parallel instabilities. The solid lines in (a) represent constant growth rates for the proton-cyclotron instability, while the dotted lines represent the parallel-firehose instability. The dashed lines in (b) show the mirror instability, while the dot-dashed lines show the oblique-firehose instability. Each value of $\tilde{p}(\beta_{\parallel p}, R_p)$ estimates the value of $p(\beta_{\parallel p}, R_p)$, or the probability density of observing a given set of $(\beta_{\parallel p}, R_p)$ -values.

3. Results

3.1. Probability Distributions of $(\beta_{\parallel p}, R_p)$ -Values

Due to the solar wind's strong magnetic field, the transport of energy is direction dependent, which can bring about temperature anisotropy. The temperature anisotropy in protons can be described by the following ratio.

$$R_p = \frac{T_{\perp p}}{T_{\parallel p}} \quad (1)$$

where R_p is the ratio of the proton temperature component perpendicular to the local mean magnetic field ($T_{\perp p}$) to the proton temperature component parallel to the magnetic field ($T_{\parallel p}$). The distribution of R_p values observed in the solar wind depend strongly on the ratio of the parallel proton pressure to the magnetic pressure, known as the parallel plasma beta (Maruca et al., 2018).

$$\beta_{\parallel p} = \frac{n_p k_B T_{\parallel p}}{|\vec{B}_{sw}|^2 / (2\mu_0)} \quad (2)$$

where n_p is the proton density, k_B is the Boltzmann constant, and μ_0 is the vacuum permeability.

A R_p value of 1 corresponds to temperature isotropy (i.e., a state of equilibrium). If R_p deviates from unity, proton temperature anisotropy may prompt various plasma instabilities. Some commonly known instabilities such as the proton-cyclotron instability and/or the mirror instability arise when the perpendicular proton temperature component is larger than the parallel proton temperature component ($T_{\perp p} > T_{\parallel p}$). However, when the parallel proton temperature component is larger than the perpendicular proton temperature component ($T_{\parallel p} > T_{\perp p}$), the parallel and/or the oblique firehose instabilities may arise.

To search for the effects of various instabilities, the approach outlined in Maruca et al. (2018) was used to plot the distribution of observations over the $(\beta_{\parallel p}, R_p)$ -plane using Equations 1 and 2. The $(\beta_{\parallel p}, R_p)$ -plane is a tool to study the impact of anisotropy-driven instabilities on protons in the solar wind.

Figure 1 displays the estimated probability density (\tilde{p}) of $(\beta_{\parallel p}, R_p)$ -values for the entire study, where

$$\tilde{p}(\beta_{\parallel p}, R_p) = \frac{n}{N \Delta \beta_{\parallel p} \Delta R_p} \quad (3)$$

here n is the number of data in a bin, N is the total amount of data in the data set, and $\Delta\beta_{\parallel p}$ and ΔR_p are the widths of the bins along each axis. Bins with $n < 10$ data were considered to be statistically insignificant and therefore were not included.

Figure 2 displays $\tilde{p}(\beta_{\parallel p}, R_p)$ for each season. The data set size (N) for Fall was 70,220 (35,110 R_p values, and 35,110 $\beta_{\parallel p}$ values). Winter contained a total data set of 57,180 points, Spring had 60,290 data points, and Summer had 41,254 total data points. The overlaid curves in both figures show the contours of constant growth rate (γ) for different instabilities normalized by the proton frequency (Ω_p). Following the method originally outlined in Maruca et al. (2011), the growth rate of an instability is taken to be the growth rate of its fastest-growing wave mode. An instability is defined as being active if wave modes are growing ($\gamma > 0$). Growth rates of anisotropy-driven instabilities are dependent upon $\beta_{\parallel p}$ and R_p values. Therefore a common analysis technique is to plot contours of constant γ in the $(\beta_{\parallel p}, R_p)$ -plane. The value $\gamma(\beta_{\parallel p}, R_p)$ is taken to be the growth rate of the fastest-growing mode for that set of values and is normalized to the proton frequency ($\Omega_p = q_p B/m_p$) where q_p is the charge and m_p the mass of a proton. All of these contours were calculated using the linear Vlasov software described by Maruca et al. (2012), which considers an idealized plasma where each population of particles has a biMaxwellian velocity distribution function. For the present study, electrons were assumed to be isotropic. Likewise, proton beams and α -particles were neglected.

The probability distributions of $(\beta_{\parallel p}, R_p)$ -values found for January 2015–December 2016 (Figure 1) closely align to distributions of interplanetary solar wind, such as in Hellinger et al. (2006), and those found in the Earth's magnetosheath, such as in Maruca et al. (2018). In all cases, as $\beta_{\parallel p}$ increases, R_p tends toward unity. This suggests that present in the upstream solar wind around Mars are processes that favor isotropic proton temperatures. Based on visual inspection of Figure 1, for $R_p > 1$ values, the proton-cyclotron instability growth rate contours appear to align better with the probability distributions of $(\beta_{\parallel p}, R_p)$ compared to the mirror instability contours. The same can be said for Fall (Figure 2a), Winter (Figure 2c), and Summer (Figure 2g). The exception being Spring (Figure 2f), where the sharper fall-off of the mirror instability contours fit the probability distribution better.

For Fall, Winter, Spring, and Summer the most common R_p values (the mathematical mode) were between 0.80–0.85, 0.70–0.80, 0.70–0.75, and 0.60–0.65, respectfully. R_p values as a function of L_s can be viewed in Plot 1 of the Supporting Information S1. The percentage of R_p values less than 1, between 1 and 1.5, and greater than 1.5 for each season are as follows. Fall: 58.31%, 25.17%, and 16.52%. Winter: 57.54%, 30.72%, and 11.74%. Spring: 70.77%, 21.97%, and 7.26%. Summer: 58.43%, 23.39%, and 18.18%. It can therefore be stated that Summer and Fall experienced the highest percentage of R_p values greater than 1.5, with Summer containing a slightly higher percentage.

3.2. Intermittency and Spectral Indices

The study of temperature anisotropy in conjunction with turbulence at Mars' orbital location was motivated by such studies as Osman et al. (2012, 2014). The authors provided evidence that a turbulent cascade from inertial to kinetic scales is the causal agent allowing the solar wind to populate the extremes of the $(\beta_{\parallel p}, R_p)$ -plane. They suggested that while instabilities may act to confine the solar wind plasma, turbulent fluctuations and cascade rates can cause temperature anisotropies, intermittent structures, and heating in the $(\beta_{\parallel p}, R_p)$ -plane.

Intermittent structures are a feature of turbulence. One way to quantify intermittency of turbulence is to calculate the PDF. Numerous studies concerned with the statistical description of solar wind magnetic field fluctuations (see the introduction of Padhye et al., 2001 and references therein) have shown that departures from Gaussianity signify intermittent structures. By taking the increments of the magnetic field components ($\delta B_i(t, \tau) = B_i(t) - B_i(t + \tau)$), we can highlight the intermittent structures present such as high magnetic stress and coherent structures (Osman et al., 2012; Parashar et al., 2015; Sorriso-Valvo et al., 1999). Here the subscript i represents the x , y , or z magnetic field component, and τ represents the time lag. Figure 3 displays the normalized PDFs of magnetic field fluctuations for each Martian season. The original magnetic field data was averaged over 1s intervals to use for PDF calculation. The PDF of the difference ($\delta B_i(t + \tau) - B_i(t)$) was then computed for a normal distribution using the mean ($\langle \delta B_i(t, \tau) \rangle$) and the standard deviation (σ_i) for each component. A time lag of 1s ($\tau = 1$) was used for two main reasons. The first being that $\tau = 1$ is of

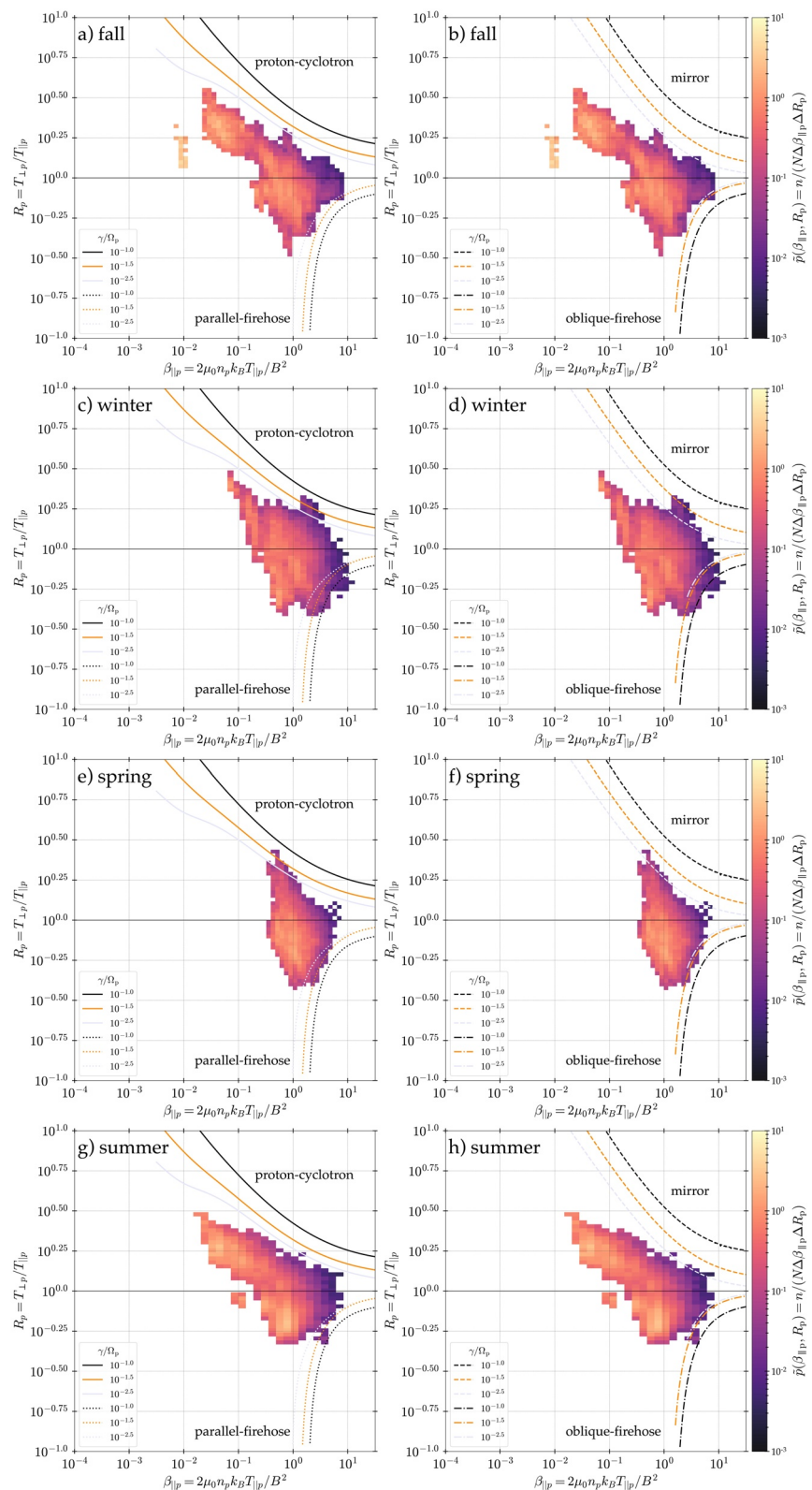


Figure 2. Probability distributions of $(\beta_{||p}, R_p)$ -values for each Martian southern hemisphere season examined. Plots (a), (c), (e), and (g) display parallel instability contours for Fall, Winter, Spring, and Summer. Plots (b), (d), (f), and (h) display perpendicular instability contours for Fall, Winter, Spring, and Summer.

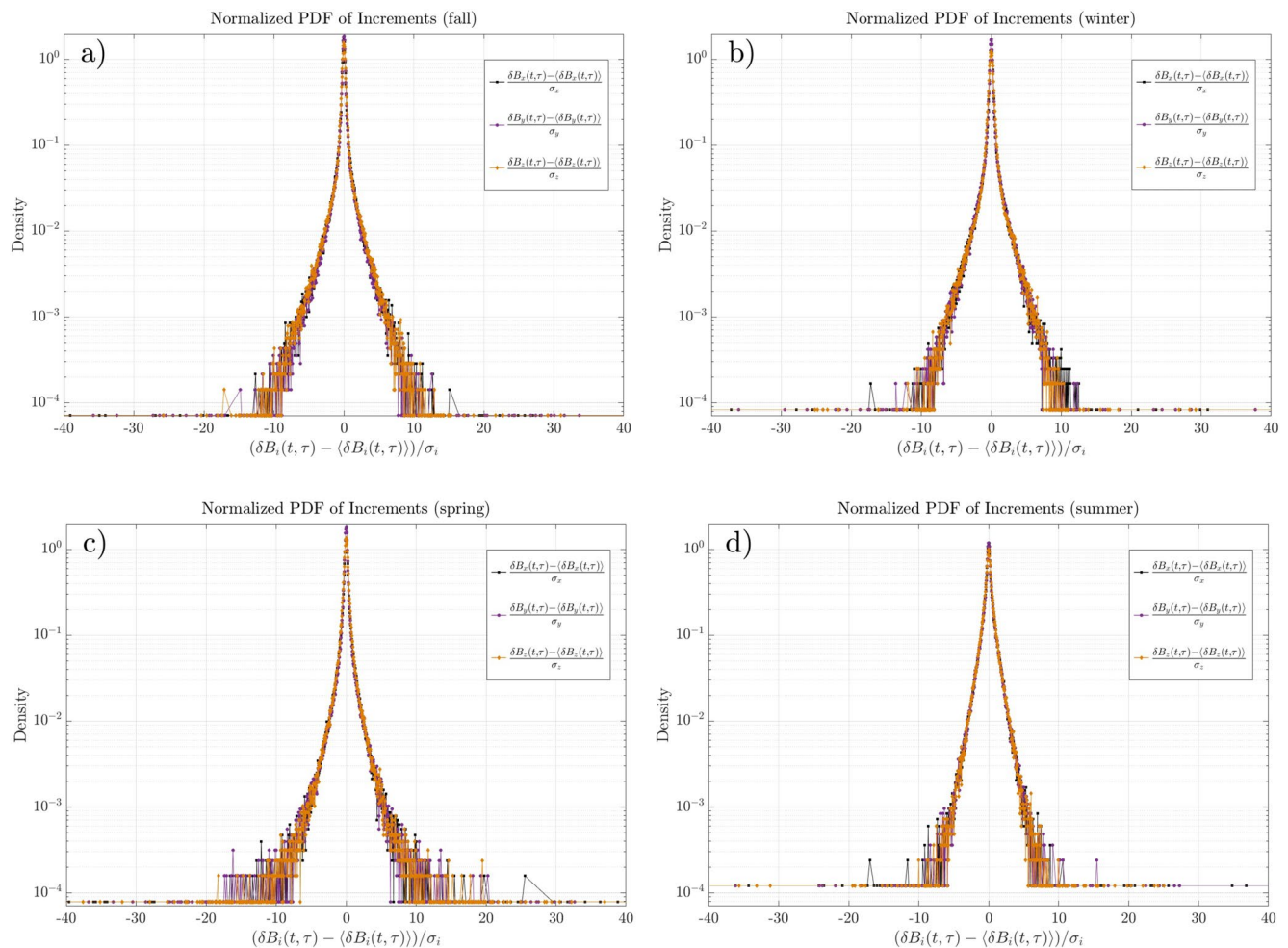


Figure 3. Seasonal normalized Probability Distribution Functions (PDF) of increments computed for the 1s averaged upstream magnetic field data for each Martian season. In each plot, all of the normalized PDF of increments for the x component of the magnetic field is plotted in black, the y component is plotted in purple, and the z component is plotted in orange. The standard deviation of $\delta B_i(t, \tau)$ is expressed as σ_i .

the order of the ion gyroradius. Second, it is comparable to the typical scale of intermittent structures (e.g., current sheets) commonly seen in solar wind turbulence. These new time series were then normalized for ease of comparison by subtracting the mean, and dividing by the standard deviation.

The inertial range solar wind PDF is known to have a typical shape with a narrow peak and over-populated tails (Marsch & Tu, 1997). The strength of the gradients highlighted depends on the lag τ . Smaller values of τ help highlight gradients (i.e., intermittent structures). When τ becomes comparable to the correlation length of the system, the PDFs revert back to Gaussianity. It has been shown that the non-Gaussian tails on the PDF of increments correspond to the number of intermittent structures (e.g., Greco et al., 2008, 2009; Salem et al., 2009; Wan et al., 2010). The examination of the PDF of magnetic field increments in Figure 3 reveals the appearance of extended tails. Of note are the relatively over-populated tails present in the Spring PDF of increments (Figure 3c), suggesting that numerous intermittent structures are present. All PDF of increments show little variation between the x , y , and z components of the magnetic field. Fall and Winter display almost identically shaped distributions. The non-Gaussianity of the PDF of increments for each season signifies the presence of intense, phase correlated fluctuations due to the transfer of energy between contiguous eddies. The intermittency observed implies that a nonlinear, non-homogeneous energy transfer is going on.

Figure 4 shows the PSD of the magnetic field fluctuations for each Martian season. To compute the PSD of magnetic field fluctuations, the fast Fourier transform (FFT) is calculated for \tilde{B}_x , \tilde{B}_y , and \tilde{B}_z . The average of

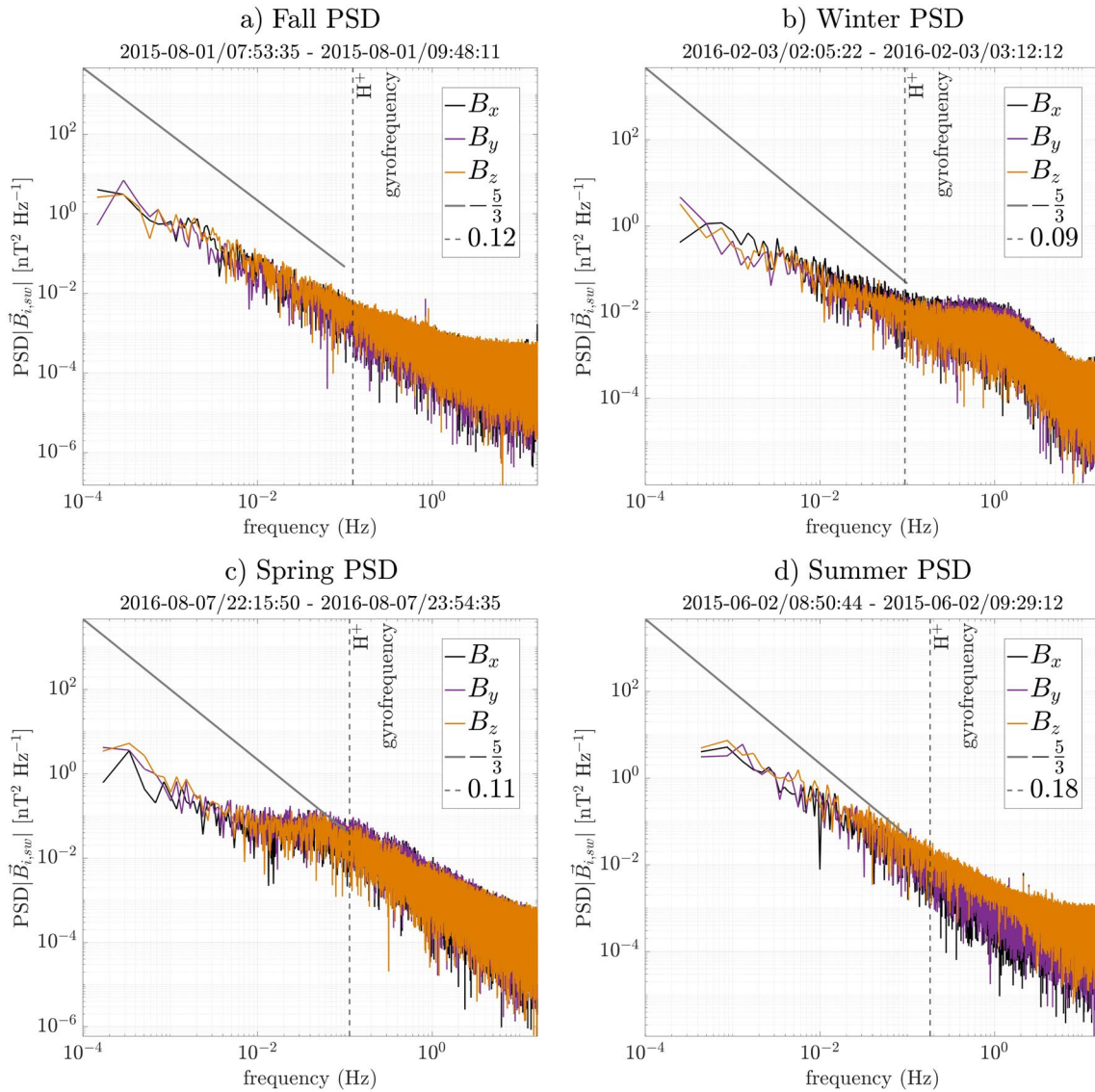


Figure 4. Magnetic Power Spectral Densities (PSD) for solar wind intervals during each Martian season. Included in each plot is the $-5/3$ Kolmogorov spectral index for the inertial range (gray line). The H^+ gyrofrequency value for each time interval is displayed in the legend, and is plotted as a vertical dashed line. Time periods shown were chosen to best represent the median spectral index calculated for each season.

each component was then subtracted from the FFT. In the study of fluid turbulence, different spatial ranges are considered. Zimbardo et al. (2010) describes the energy containing range, injection scale, inertial range, and dissipation scale that are used in magnetized plasmas. Only the inertial range is covered in this study. Via different mechanisms (see e.g., Section 2 of Zimbardo et al., 2010), energy is injected into the system and subsequently transferred to smaller and smaller scales. The transfer is best described by a power-law turbulence spectrum ($E_k \propto k^{-\alpha}$) where E_k is the power spectral density at wavenumber k , and α is the spectral index. The inertial range is between 10^{-4} Hz to 0.1 Hz, and in solar wind, has an α of $-5/3$. This line is plotted for reference in gray in Figure 4. The H^+ gyrofrequency calculated for each time interval is plotted as a vertical dashed line, with its value listed in the legend. For each solar wind interval, the spectral index was found by fitting the PSD to the form ax^b , where b represents the spectral index. Only the inertial range frequency segment of the PSD was fit. This produced a spectral index for every upstream solar wind period. The PSDs plotted in Figure 4 were chosen to represent the median spectral index found for each season. The Fall, Winter, Spring, and Summer median spectral indices were as follows, -1.20 , -1.11 , -1.08 , and -1.57 . The median spectral index for the inertial range during summer time periods is very close to the

classic Kolmogorov spectral index. This suggests that we did indeed observe mainly solar wind magnetic turbulence. The plasma encountered during the rest of the seasons exhibited power spectra of magnetic field fluctuations characterized by power law decays. The less negative spectral indices found during Fall, Winter, and Spring imply a fast transfer of energy to small scales. When looking at the distribution of the spectral indices found for each season, there was a general trend between the length of the upstream solar wind interval identified, and the value of the spectral index. It was found that for shorter time intervals, spectral indices took on larger values.

4. Discussion

This article examines the temperature anisotropy and associated instabilities present around Mars' orbital location. The basic characteristics of magnetic turbulence are also studied in order to compare to known interplanetary solar wind characteristics. Figures 1 and 2 demonstrate that, as in the case of Earth's magnetosheath, there exists processes that favor isotropic proton temperatures and become more active at higher values of $\beta_{\parallel p}$. The proton temperature anisotropies found upstream of Mars are confined to a constrained parameter space, shaped by the presence of kinetic instabilities. Fall, Winter, and Summer saw ~58% of their total R_p values fall below 1 ($T_{\perp p} < T_{\parallel p}$). Approximately 71% of Spring R_p values were below 1. This can either be due to the parallel propagating firehose instability or the oblique-firehose instability. Both instabilities can be present simultaneously and show comparable growth rates. It is unclear which instability dominates in limiting the observed temperature anisotropies. Based on visual inspection alone, plasma with a perpendicular temperature anisotropy ($R_p > 1$) appears to be unstable to proton-cyclotron waves, as previously mentioned in the analysis of Figures 1 and 2. Spring is excluded, where it appears as though the sharper fall-off of the mirror instability contours fit the probability distribution better. Observations made during this study of upstream protons indicate that their most common anisotropic condition is $T_{\perp p}/T_{\parallel p} < 1$.

Figure 3 demonstrates peaked and long-tailed non-Gaussian distributions, showing the presence of intermittency. This implies a nonlinear, non homogeneous energy transfer is going on. Spring demonstrated the most solar wind-like distribution, whereas Fall, Winter, and Summer contained less populated tails. Examining Figure 4d, the median spectral index for the inertial range during the Summer time periods was closest to the classic Kolmogorov spectral index (−1.67). A caveat of studying turbulence in upstream solar wind around Mars is the time length of intervals. It is not possible to obtain continuous upstream solar wind measurements for more than a couple of hours. To study fully developed turbulence, it is desirable for data to cover at least one decade in frequency space (Burlaga, 1991). The absence of the inertial range with the Kolmogorov scaling value for Fall, Winter, and Spring can be a direct result of this. During short intervals, the PSD of the magnetic field did not span all inertial range frequencies, and the resulting spectral indices did not fully characterize the turbulence in the Mars plasma environment. Expanding this same study to multiple years worth of data would aid in a more conclusive analysis of the seasonal variation of spectral indices and intermittency.

Lengthier and more numerous time periods are needed to decouple the impact of the Martian exosphere on R_p values. Endeavors to determine systematic differences in temperature anisotropy that can be accounted for by seasonal variability would also be of interest. Alpha particles, although less abundant, are a non-negligible ion species. The possibility of further instabilities triggered by alpha particles was beyond the scope of this study, but would contribute to the study of turbulence. The results of this preliminary study motivate further investigations into how temperature anisotropy constraints arise in Martian exosphere and how they impact the large-scale evolution of the plasma.

Data Availability Statement

The MAVEN data shown are publicly available at the NASA Planetary Data System website (<http://ppi.pds.nasa.gov>).

Acknowledgments

The MAVEN mission has been made possible through NASA sponsorship and the dedicated efforts of NASA Goddard Space Flight Center, LASP, Lockheed Martin, and the MAVEN Technical and Science Teams.

References

- Anderson, D. E. (1974). Mariner 6, 7, and 9 ultraviolet spectrometer experiment: Analysis of hydrogen lyman alpha data. *Journal of Geophysical Research*, 79(10), 1513–1518. <https://doi.org/10.1029/JA079i010p01513>
- Anderson, D. E., & Hord, C. W. (1971). Mariner 6 and 7 ultraviolet spectrometer experiment: Analysis of hydrogen lyman-alpha data. *Journal of Geophysical Research*, 76(28), 6666–6673. <https://doi.org/10.1029/JA076i028p06666>
- Andrés, N., Romanelli, N., Hadid, L. Z., Sahraoui, F., DiBraccio, G., & Halekas, J. (2020). Solar wind turbulence around mars: Relation between the energy cascade rate and the proton cyclotron waves activity. *The Astrophysical Journal*, 902, 134–143. <https://doi.org/10.3847/1538-4357/abb5a7>
- Bhattacharyya, D., Clarke, J. T., Chaufray, J. Y., Mayyasi, M., Bertaux, J. L., Chaffin, M. S., et al. (2017). Seasonal changes in hydrogen escape from mars through analysis of hst observations of the Martian exosphere near perihelion. *Journal of Geophysical Research: Space Physics*, 122(11), 11756–11764. <https://doi.org/10.1002/2017JA024572>
- Bruno, R., & Carbone, V. (2016). *Turbulence in the solar wind*. Springer. <https://doi.org/10.1007/978-3-319-43440-7>
- Burlaga, L. F. (1991). Intermittent turbulence in the solar wind. *Journal of Geophysical Research*, 96(A4), 5847–5851. <https://doi.org/10.1029/91JA00087>
- Chaffin, M. S., Chaufray, J. Y., Deighan, J., Schneider, N. M., McClintock, W. E., Stewart, A. I. F., et al. (2015). Three-dimensional structure in the Mars h corona revealed by iuvms on maven. *Geophysical Research Letters*, 42(21), 9001–9008. <https://doi.org/10.1002/2015GL065287>
- Chaufray, J., Bertaux, J., Leblanc, F., & Quémerais, E. (2008). Observation of the hydrogen corona with spicam on Mars express. *Icarus*, 195(2), 598–613. <https://doi.org/10.1016/j.icarus.2008.01.009>
- Connerney, J. E. P., Espley, J., Lawton, P., Murphy, S., Odom, J., Oliverson, R., & Sheppard, D. (2015). The maven magnetic field investigation. *Space Science Reviews*, 195, 257–291. <https://doi.org/10.1007/s11214-015-0169-4>
- Espley, J. R. (2018). The Martian magnetosphere: Areas of unsettled terminology. *Journal of Geophysical Research: Space Physics*, 123(6), 4521–4525. <https://doi.org/10.1029/2018JA025278>
- Greco, A., Chuychai, P., Matthaeus, W. H., Servidio, S., & Dmitruk, P. (2008). Intermittent mhd structures and classical discontinuities. *Geophysical Research Letters*, 35(19), L19111. <https://doi.org/10.1029/2008GL035454>
- Greco, A., Matthaeus, W. H., Servidio, S., Chuychai, P., & Dmitruk, P. (2009). Statistical analysis of discontinuities in solar wind ace data and comparison with intermittent mhd turbulence. *The Astrophysical Journal*, 691(2), L111–L114. <https://doi.org/10.1088/0004-637x/691/2/L111>
- Halekas, J. S. (2017). Seasonal variability of the hydrogen exosphere of mars. *Journal of Geophysical Research: Planets*, 122, 901–911. <https://doi.org/10.1002/2017JE005306>
- Halekas, J. S., Ruhunusiri, S., Harada, Y., Collinson, G., Mitchell, D. L., Mazelle, C., et al. (2017). Structure, dynamics, and seasonal variability of the Mars-solar wind interaction: Maven solar wind ion analyzer in-flight performance and science results. *Journal of Geophysical Research: Space Physics*, 122(1), 547–578. <https://doi.org/10.1002/2016JA023167>
- Halekas, J. S., Taylor, E. R., Dalton, G., Johnson, G., Curtis, D. W., McFadden, J. P., et al. (2015). The solar wind ion analyzer for maven. *Space Science Reviews*, 195, 125–151. <https://doi.org/10.1007/s11214-013-0029-z>
- Hellinger, P., Trávníček, P., Kasper, J. C., & Lazarus, A. J. (2006). Solar wind proton temperature anisotropy: Linear theory and wind/swe observations. *Geophysical Research Letters*, 33(9), L09101. <https://doi.org/10.1029/2006GL025925>
- Horbury, T. S., Forman, M., & Oughton, S. (2008). Anisotropic scaling of magnetohydrodynamic turbulence. *Physical Review Letters*, 101, 175005. <https://doi.org/10.1103/PhysRevLett.101.175005>
- Howes, G. G. (2008). Inertial range turbulence in kinetic plasmas. *Physics of Plasmas*, 15(5), 055904. <https://doi.org/10.1063/1.2889005>
- Klein, K. G., & Howes, G. G. (2015). Predicted impacts of proton temperature anisotropy on solar wind turbulence. *Physics of Plasmas*, 22(3), 032903. <https://doi.org/10.1063/1.4914933>
- Kolmogorov, A. (1941a). The local structure of turbulence in incompressible viscous fluid for very large Reynolds' numbers. *Akademiia Nauk SSSR Doklady*, 30, 301–305.
- Kolmogorov, A. N. (1941b). Dissipation of energy in locally isotropic turbulence. *Akademiia Nauk SSSR Doklady*, 32, 16.
- Liu, D., Rong, Z., Gao, J., He, J., Klinger, L., Dunlop, M. W., et al. (2021). Statistical properties of solar wind upstream of mars: MAVEN observations. *The Astrophysical Journal*, 911(2), 113. <https://doi.org/10.3847/1538-4357/abed50>
- Luhmann, J. (1992). Comparative studies of the solar wind interaction with weakly magnetized planets. *Advances in Space Research*, 12(9), 191–203. [https://doi.org/10.1016/0273-1177\(92\)90331-Q](https://doi.org/10.1016/0273-1177(92)90331-Q)
- Marsch, E., & Tu, C.-Y. (1997). Intermittency, non-Gaussian statistics and fractal scaling of mhd fluctuations in the solar wind. *Nonlinear Processes in Geophysics*, 4(2), 101–124. <https://doi.org/10.5194/npg-4-101-1997>
- Maruca, B. A., Chasapis, A., Gary, S. P., Bandyopadhyay, R., Chhiber, R., Parashar, T. N., et al. (2018). Mms observations of beta-dependent constraints on ion temperature anisotropy in Earth's magnetosheath. *The Astrophysical Journal*, 866, 25–30. <https://doi.org/10.3847/1538-4357/aadfb>
- Maruca, B. A., Kasper, J. C., & Bale, S. D. (2011). What are the relative roles of heating and cooling in generating solar wind temperature anisotropies? *Physical Review Letters*, 107, 201101. <https://doi.org/10.1103/PhysRevLett.107.201101>
- Maruca, B. A., Kasper, J. C., & Gary, S. P. (2012). Instability-driven limits on helium temperature anisotropy in the solar wind: Observations and linear vlasov analysis. *The Astrophysical Journal*, 748, 137–143. <https://doi.org/10.1088/0004-637X/748/2/137>
- Matteini, L., Landi, S., Hellinger, P., Pantellini, F., Maksimovic, M., Velli, M., & Marsch, E. (2007). Evolution of the solar wind proton temperature anisotropy from 0.3 to 2.5 au. *Geophysical Research Letters*, 34(20), L20105. <https://doi.org/10.1029/2007GL030920>
- Matthaeus, W. H., & Goldstein, M. L. (1982). Measurement of the rugged invariants of magnetohydrodynamic turbulence in the solar wind. *Journal of Geophysical Research*, 87(A8), 6011–6028. <https://doi.org/10.1029/JA087iA08p06011>
- Mazelle, C., Winterhalter, D., Sauer, K., Trotignon, J., Acuña, M., Baumgärtel, K., et al. (2004). Bow shock and upstream phenomena at Mars. *Space Science Reviews*, 111, 115–181. <https://doi.org/10.1023/B:SPAC.0000032717.98679.d0>
- Osman, K. T., Matthaeus, W. H., Gosling, J. T., Greco, A., Servidio, S., Hnat, B., & Phan, T. D. (2014). Magnetic reconnection and intermittent turbulence in the solar wind. *Physical Review Letters*, 112, 215002–215007. <https://doi.org/10.1103/PhysRevLett.112.215002>
- Osman, K. T., Matthaeus, W. H., Hnat, B., & Chapman, S. C. (2012). Kinetic signatures and intermittent turbulence in the solar wind plasma. *Physical Review Letters*, 108, 261103–261107. <https://doi.org/10.1103/PhysRevLett.108.261103>
- Padhye, N. S., Smith, C. W., & Matthaeus, W. H. (2001). Distribution of magnetic field components in the solar wind plasma. *Journal of Geophysical Research*, 106(A9), 18635–18650. <https://doi.org/10.1029/2000JA000293>
- Parashar, T. N., Salem, C., Wicks, R. T., Karimabadi, H., Gary, S. P., & Matthaeus, W. H. (2015). Turbulent dissipation challenge: A community-driven effort. *Journal of Plasma Physics*, 81(5), 905810513. <https://doi.org/10.1017/S0022377815000860>

- Pine, Z. B., Smith, C. W., Hollick, S. J., Argall, M. R., Vasquez, B. J., Isenberg, P. A., et al. (2020). Solar wind turbulence from 1 to 45 au. iv. Turbulent transport and heating of the solar wind using voyager observations. *The Astrophysical Journal*, 900(2), 91–102. <https://doi.org/10.3847/1538-4357/abab12>
- Ruhunusiri, S., Halekas, J. S., Espley, J. R., Mazelle, C., Brain, D., Harada, Y., et al. (2017). Characterization of turbulence in the Mars plasma environment with maven observations. *Journal of Geophysical Research: Space Physics*, 122(1), 656–674. <https://doi.org/10.1002/2016JA023456>
- Salem, C., Mangeney, A., Bale, S. D., & Veltri, P. (2009). Solar wind magnetohydrodynamics turbulence: Anomalous scaling and role of intermittency. *The Astrophysical Journal*, 702(1), 537–553. <https://doi.org/10.1088/0004-637x/702/1/537>
- Sorriso-Valvo, L., Carbone, V., Veltri, P., Consolini, G., & Bruno, R. (1999). Intermittency in the solar wind turbulence through probability distribution functions of fluctuations. *Geophysical Research Letters*, 26(13), 1801–1804. <https://doi.org/10.1029/1999GL900270>
- Verscharen, D., Klein, K. G., & Maruca, B. A. (2019). The multi-scale nature of the solar wind. *Living Reviews in Solar Physics*, 16, 5. <https://doi.org/10.1007/s41116-019-0021-0>
- Wan, M., Oughton, S., Servidio, S., & Matthaeus, W. H. (2010). On the accuracy of simulations of turbulence. *Physics of Plasmas*, 17(8), 082308. <https://doi.org/10.1063/1.3474957>
- Zimbardo, G., Greco, A., Sorriso-Valvo, L., Perri, S., Vörös, Z., Aburjania, G., & Alexandrova, O. (2010). Magnetic turbulence in the geo-space environment. *Space Science Reviews*, 156, 89–134. <https://doi.org/10.1007/s11214-010-9692-5>